remote sensing

MDPI

Article

Coupled Mechanisms Between Permafrost Degradation and Vegetation Dynamics in a Typical Alpine Catchment of the Qilian Mountains over the Past Four Decades

Xuhui Wang [1,2], Qiang Gu [1,3], Xuyang Wu [2], Xinyi Liu [2], Xiaocui Zhou [2], Zhanju Lin [2] and Xingwen Fan [1,2,*]

[1] Observation Station of Subalpine Ecology Systems in the Middle Qilian Mountains, China Geological Survey (CGS), Xining 810099, China; wangxuhui@nieer.ac.cn (X.W.); cctvguqiang@163.com (Q.G.)
[2] Key Laboratory of Cryospheric Science and Frozen Soil Engineering, Chinese Academy of Sciences, Lanzhou 730000, China; wuxuyang@nieer.ac.cn (X.W.); liuxinyi261@mails.ucas.ac.cn (X.L.); zhouxiaocui25@mails.ucas.ac.cn (X.Z.); zhanjulin@lzb.ac.cn (Z.L.)
[3] Xining Integrated Natural Resources Centre, China Geological Survey, Xining 810099, China
* Correspondence: fanxingwen18@mails.ucas.ac.cn

Highlights

What are the main findings?

- Permafrost area in a typical Qilian Mountains catchment shrank from 92.5% to 73.8% over 1986–2025, with stage-wise accelerated degradation.
- Vegetation greening peaks when active layer deepens to an optimal threshold of approximately 1.2 m.

What are the implications of the main findings?

- Climate–permafrost cascading effects dominate long-term alpine ecosystem evolution; current greening benefits from hydrothermal conditions released during initial permafrost degradation.
- Continued ground-ice depletion may weaken the current thermal benefit to vegetation.

Abstract

Under a warming climate, the impact of alpine permafrost degradation on vegetation dynamics is crucial for understanding ecosystem evolution. Drawing on long-term multi-source observational data from 1986 to 2025 and Structural Equation Modeling (SEM), this study investigated the coupled mechanisms between permafrost degradation and vegetation dynamics in a typical alpine catchment of the Qilian Mountains. The results demonstrated that: (1) Over the past four decades, permafrost in the study area exhibited a continuous degradation pattern, with its areal extent decreasing from 92.5% to 73.8% at a rate of approximately 0.53% yr^{-1}. This degradation was characterized by spatial heterogeneity, showing preferential degradation in the southern region and intensified fragmentation in the central region. (2) The study area experienced an overall significant greening trend. Between 2021 and 2025, areas with high vegetation coverage (Normalized Difference Vegetation Index (NDVI) ≥ 0.09) accounted for 66.4% of the total area, and the greening rate was significantly but only partly modulated by local topography. (3) The permafrost thermal regime exerted a pronounced gradient effect on vegetation dynamics. Vegetation improvement was most rapid in Degraded Permafrost zones, and the promoting effect of active layer deepening on vegetation growth exhibited an optimal threshold of approximately 1.2 m. (4) The freeze-state index showed the strongest statistical association with vegetation dynamics ($\beta = -0.56$), whereas the direct precipitation effect was negligible ($\beta = -0.01$); the two climate variables co-vary along the elevational gradient and cannot

Check for updates

Academic Editor: Ulrich Kamp

Received: 5 October 2026
Revised: 7 November 2026
Accepted: 12 November 2026
Published: 17 November 2026

Copyright: © 2026 by the authors. Licensee MDPI, Basel, Switzerland. This article is an open access article distributed under the terms and conditions of the Creative Commons Attribution (CC BY) license.

be separated here. Current greening has benefited from hydrothermal conditions released during early permafrost degradation, but this effect may weaken as ground ice is depleted.

Keywords: permafrost degradation; NDVI; Qilian Mountains; alpine ecosystem; remote sensing

1. Introduction

The Qinghai–Tibet Plateau (QTP) is the highest and most extensive alpine eco-geographical unit globally, harboring the largest concentration of permafrost in the low- and mid-latitudes. The intricate interplay among permafrost, seasonally frozen ground, alpine meadows, alpine steppes, and alpine wetlands constitutes the unique cold-region ecosystem of the plateau. Permafrost thaw serves not only as a crucial indicator of climate change but also regulates soil temperature, active layer thickness (ALT), and soil moisture migration, thereby controlling the hydrothermal and nutrient conditions available to alpine vegetation. Covering an area of approximately 1.08 million km^2, permafrost on the QTP profoundly impacts the ecological security, water conservation, and carbon cycling of the region [1–4].

Over the past few decades, permafrost temperatures on the QTP have risen significantly, accompanied by a continuous increase in ALT. The permafrost area decreased from $1.262 \pm 0.048 \times 10^6$ km^2 in 1980 to $1.085 \pm 0.049 \times 10^6$ km^2 in 2018, representing a total loss of approximately 1.77×10^5 km^2. Concurrently, the active layer deepened at a rate of 0.04 m per decade, the permafrost table warmed by 0.10 °C per decade, and the depth of zero annual amplitude (DZAA) moved upward by 0.52 m per decade [2]. Given that QTP permafrost is generally characterized by relatively high ground temperatures, poor thermal stability, and high sensitivity to external disturbances, its degradation involves more than merely alterations in its own thermal regime. It also triggers cascading effects on alpine ecosystems by altering surface water-groundwater connectivity, soil moisture migration pathways, and root-zone hydrothermal conditions [5,6].

Vegetation is both a sensitive responder to permafrost environmental changes and a critical land surface factor that modulates the permafrost thermal regime. As permafrost degrades and the active layer deepens, the impact of permafrost degradation on vegetation is not a simple unidirectional facilitation or inhibition. Instead, it exhibits a stage-dependent transition, typically shifting from an initial "warming and wetting effect" to a subsequent "drainage and drying effect" [7–9]. The thickening of the active layer allows organic matter and inorganic nutrients, previously sequestered in deep frozen soils, to enter the seasonal thaw layer. This process accelerates microbial decomposition and the mineralization of elements such as nitrogen and phosphorus, thereby increasing nutrient availability for certain plants. Deep-rooted plants can utilize the inorganic nitrogen released by permafrost thaw, granting them a competitive advantage within the community and consequently driving shifts in plant functional types and species composition [10]. Conversely, vegetation-induced effects—such as summer shading, winter snow trapping, altered evapotranspiration, and changes in surface albedo—can exert opposing thermal impacts on the soil. The net effect heavily depends on plant functional types, seasonality, and the regional hydrothermal background [11–13].

At the regional scale, the interactions between permafrost degradation and vegetation dynamics exhibit pronounced spatial heterogeneity. Studies in the source region of the Yellow River have shown that permafrost degradation deepens groundwater circulation pathways, lowers the supra-permafrost water table, and drives the transition of humid vegetation to drought-tolerant species. Crucially, an increase in NDVI observed via remote

sensing does not necessarily equate to ecosystem recovery, as vegetation indices struggle to capture structural changes such as species turnover, weed proliferation, and community degradation [3,6]. In continuous permafrost zones and humid alpine regions, a moderate deepening of the active layer can expand the rooting space for plants and enhance vegetation productivity by promoting soil organic matter decomposition and nutrient release. However, in discontinuous permafrost zones, at the southern margins of permafrost, and in semi-arid alpine regions, permafrost degradation may weaken the aquiclude effect, leading to a declining water table and surface soil desiccation. This ultimately decelerates the growth rate of NDVI or even triggers vegetation browning [11,14,15]. Similarly, research in the Arctic tundra revealed widespread vegetation greening from 1985 to 2016, yet with uneven spatial distribution; localized browning was closely associated with snow anomalies, soil moisture limitations, wildfires, and thermokarst disturbances [16,17]. Furthermore, feedback mechanisms to permafrost vary among different plant functional types. Mosses and litter layers typically buffer active layer thaw through thermal insulation, whereas shrub expansion can elevate soil temperatures by trapping snow and reducing surface albedo. In certain plateau regions, vegetation greening may even amplify shallow soil warming [12,13,18].

Although existing studies have independently elucidated the ecological effects of permafrost degradation and the surface energy effects of vegetation changes, most research predominantly focuses on the unidirectional impacts of permafrost on vegetation or relies on statistical correlation analyses of permafrost and vegetation trends. A comprehensive understanding of their bidirectional feedback, time lags, and non-linear thresholds remains insufficient. Compared to simple correlation analyses, Structural Equation Modeling (SEM) provides a robust framework capable of disentangling the complex cascading effects between climate drivers and permafrost-vegetation variables [19]. Therefore, by integrating multi-source remote sensing datasets with newly conducted field borehole observations, this study employs SEM to systematically identify the direct and indirect pathways of permafrost-vegetation coupling. Through this approach, we seek to reveal the dominant mechanisms and their spatial heterogeneity across varying permafrost and vegetation types. Unraveling these complex interactions are of profound significance for predicting the evolutionary trajectories of alpine ecosystems on the QTP under future climate change scenarios, as well as for formulating effective strategies for permafrost conservation, grassland restoration, and ecological security management.

2. Study Area

The study area focuses on a representative local watershed in the Qilian Mountains, specifically a tributary of the Buha River, which is characterized by a typical plateau continental climate (Figure 1). The watershed covers an area of approximately 2993 km^2, spanning coordinates from 37.44° to 38.24°N and 98.57° to 99.14°E. Its vector boundary was delineated based on Digital Elevation Model (DEM) data, with the outlet located on the upper Buha River (Waha Qu) at 98.68°E, 37.45°N. The watershed is situated in an ecological transitional zone characterized by a longitudinal vegetation gradient, making the alpine vegetation here extremely sensitive to variations in climate and permafrost.

Because of the pronounced topographic relief and the strong elevational gradient, hydrothermal conditions in the study area show marked spatial heterogeneity and a clear elevation dependence. Over 1991–2020, the mean annual air temperature (MAAT) decreased from −1.8 °C in the lowest grid cells (≈3800 m) to −5.0 °C in the highest (≈4200 m), a lapse rate of approximately 0.7 °C per 100 m of elevation gain. The mean air temperatures of the coldest (January) and warmest (July) months were −18.7 to −15.2 °C and 7.4 to 10.0 °C, respectively. Based on the highest daily maximum and the lowest daily minimum

air temperature (i.e., quasi-instantaneous extremes), the extreme maximum and minimum air temperatures were 25.7 °C and −35.5 °C, respectively. The mean annual precipitation (MAP) was about 350 mm, more than 75% of which was concentrated between June and September and fell mainly as high-frequency, low-intensity events. The annual potential evapotranspiration (PET), estimated with the Hargreaves equation, was 580–710 mm, about 1.8–2.0 times MAP. The annual mean wind speed was 2.8 m s^{-1} (Beaufort force 2), and the maximum daily mean wind speed reached 9–11 m s^{-1} (force 5).

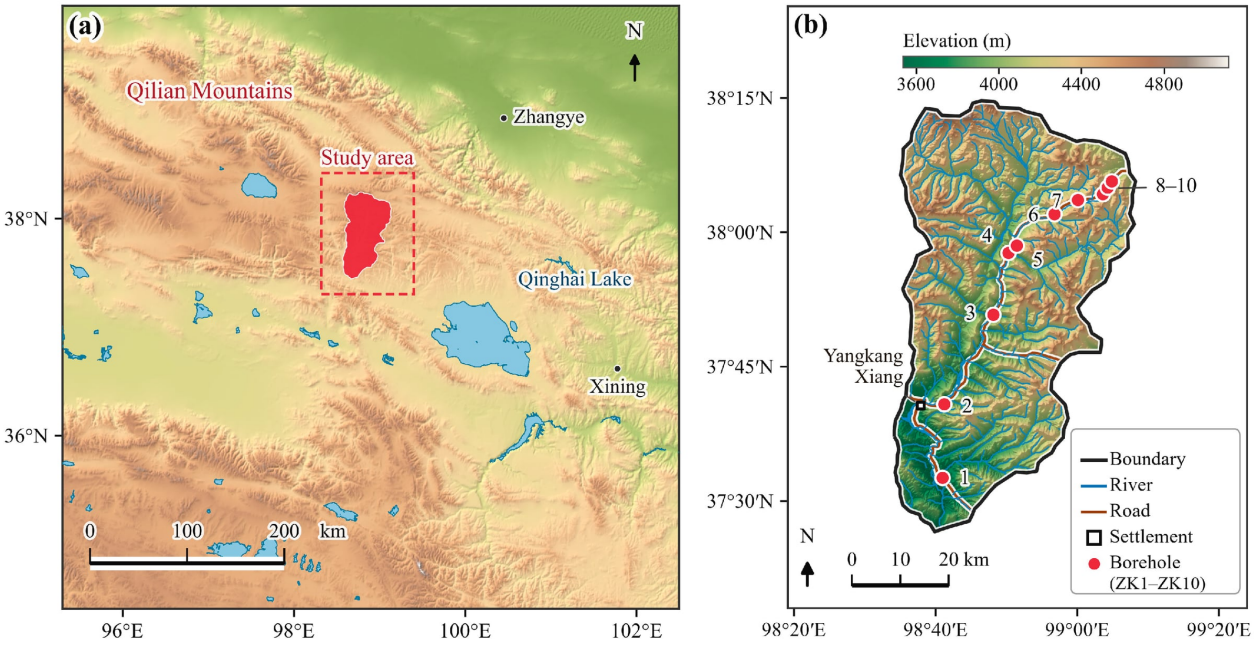

Figure 1. Location and setting of the study area. (**a**) Position of the study catchment on the northeastern Qinghai–Tibet Plateau. (**b**) Topography, drainage network and boreholes (ZK1–ZK10) of the catchment.

3. Data and Methods

3.1. Data Sources

This study integrated multi-source datasets spanning from 1986 to 2025, including meteorological, vegetation remote sensing, permafrost, and basic geographical data, to analyze the spatiotemporal evolution characteristics and coupled mechanisms of permafrost and vegetation dynamics in the study area. To ensure consistency in spatial analysis, all spatial data were standardized to a uniform projected coordinate system and clipped to the study area boundary. The specific data sources are as follows:

Climate statistics reported in Section 2 were derived from the NASA POWER (MERRA-2) reanalysis (0.5° × 0.625°, ≈55 km at 38°N; https://power.larc.nasa.gov/) using its daily and monthly fields at the nearest grid cell, without downscaling, over the 1991–2020 reference period. The values were cross-checked against monthly records from four national meteorological stations around the study area (1991–2012). These statistics describe the background climate of the catchment and are not used in the subsequent time-series analyses, which rely on the 1 km gridded datasets described below.

Air temperature and precipitation data were obtained from the high-resolution (1 km) monthly meteorological datasets archived at the National Tibetan Plateau/Third Pole Environment Data Center (TPDC, https://data.tpdc.ac.cn/) [20–23], namely the 1 km monthly mean temperature dataset for China (1901–2025) and the 1 km monthly precipitation dataset for China (1901–2025), and they were used to analyze hydrothermal variations in the study area.

Permafrost data comprised the simulated dataset of active layer thickness and ground temperature on the Qinghai–Tibet Plateau (2000–2015) and the ground temperature distribution map of the Tibet Engineering Corridor (2010–2015). These permafrost datasets were also acquired from the TPDC [24,25], providing a foundational basis for investigating the regulatory effects of permafrost and active layer changes on vegetation.

Raw remote sensing images for NDVI were acquired via the Google Earth Engine (GEE) cloud platform (https://code.earthengine.google.com/). Given the study period (1986–2025), surface reflectance datasets from Landsat 5 and Landsat 7 were utilized for the years 1986–1999, while the MODIS MOD13Q1 dataset was employed for the period 2000–2025. Detailed methods for NDVI time-series construction and image preprocessing are provided in Section 3.4.

DEM data with a spatial resolution of 100 m were downloaded from the National Geospatial Data Cloud (NGDC, https://www.gscloud.cn/) and used to extract topographic factors, including elevation, slope, and aspect, to analyze the modulatory effects of local topography on vegetation and permafrost.

3.2. Field Investigation Results

To validate the macroscopic TPDC permafrost dataset and evaluate the deep ground ice conditions, a long-term permafrost monitoring network was established along the G338 highway in 2025. The boreholes, drilled to a depth of 15 m, provide a basis for confirming the depth of the permafrost table, identifying the presence of deep stratified ice, and determining the position of the 0 °C isotherm, thereby providing crucial deep-ground physical truth for the TPDC simulation.

Ten boreholes (ZK1–ZK10) were deployed along the elevation gradient within the study area. The surface elevations of these boreholes ascend gradually from 3550 m to 4250 m before descending to 4050 m, with each borehole drilled to a depth of approximately 15 m (Figure 2). The drilling results revealed that the shallow stratigraphy of the study area exhibits distinct vertical stratification and elevation-dependent spatial heterogeneity.

The lower-elevation zone (ZK1–ZK5, 3550–3950 m) is dominated by Quaternary unconsolidated sediments with complex lithological associations, primarily comprising an alpine turf layer, sandy gravel, sand, gravel, cobbles, silty clay, clay, and peaty soil. Specifically, the upper section of ZK1 consists of a turf layer and sandy gravel, underlain by a cobble layer, silty clay, and peaty soft rock. The topsoil of ZK2 is composed of gray clay, predominantly underlain by sand and thick gravel layers. ZK3 is mainly composed of a sandy gravel layer. ZK4 exhibits a multi-layered structure of peaty clay, gravelly clay, sandy gravel, and clay. At 3950 m, ZK5 is primarily composed of gravelly clay, gravel, cobbles, and a relatively thick peat layer. These variations indicate strong heterogeneity in sediment sources and depositional environments across the low- to mid-elevation regions.

Transitioning into the high-elevation zone, the stratigraphic structure and ground ice characteristics shift significantly. In ZK6 (4050 m), the upper 3 m comprises a clay layer, underlain by a thick layer of ice-rich sandy soil featuring distinct stratified ice structures, indicative of high ground ice content in the permafrost. Beneath this ice-rich layer lie a gravel layer and limestone bedrock. ZK7 (4150 m) contains a shallow turf layer and a thick sandy gravel layer, transitioning into bedrock at a depth of approximately 8.5 m. The most prominent permafrost characteristics are observed at the highest elevation, ZK8 (4250 m). Its upper section consists of a root-bearing clay layer, with a peat layer and stratified ice developed between depths of 1.5 and 5.8 m, directly overlying the bedrock. This suggests highly favorable conditions for moisture accumulation and ground ice formation at the summit. Boreholes ZK9 and ZK10, located on the descending slope at 4150 m and 4050 m,

respectively, are overlain by relatively thin layers of root-bearing clay, gravel, or sand, with bedrock depths consistently around 6 m.

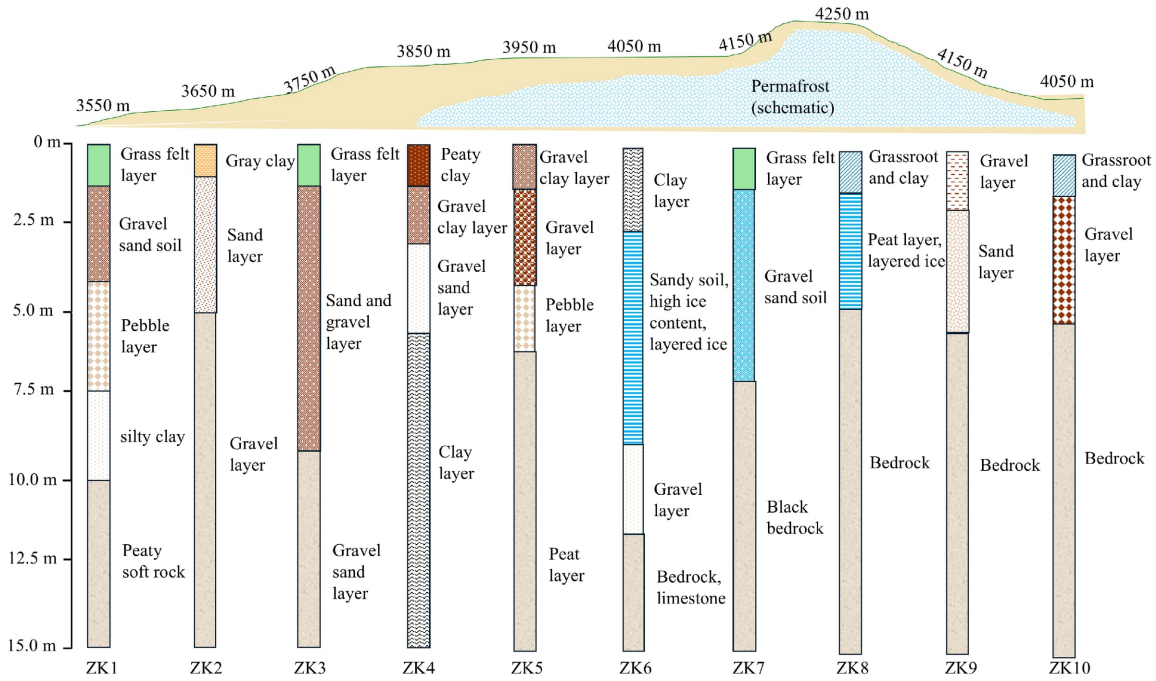

Figure 2. Drilling results of the permafrost boreholes. Lithological logs are drawn to the depth scale on the left (0–15 m). The blue area at the top is a schematic representation of the permafrost body along the profile; it is not drawn to scale, and neither its thickness nor that of the overlying active layer corresponds to measured values. Numbers along the profile are ground elevations at the borehole locations (m).

Overall, permafrost is primarily distributed in areas above 4000 m, with its lower elevational limit generally situated between 3950 and 4050 m. Concurrently, as elevation increases, the unconsolidated overburden generally thins, the depth to bedrock decreases, and ice-rich soil layers along with stratified ground ice become distinctly well-developed in high-elevation terrains. These findings reveal that the permafrost distribution and stratigraphic ground ice characteristics in the study area are co-controlled by elevation, topography, and lithological conditions.

3.3. Calculation Methods for Permafrost Changes

The extraction of air freezing and thawing indices, as well as the determination of the spatial distribution of permafrost in this study, were conducted following the research framework of Wang et al. [26]. This study extracted the F-index, defined as the ratio of the air freezing index to the thawing index within the calculation period.

3.4. NDVI Calculation Methods

This study utilized two sets of remote sensing products to piecewise construct the annual mean NDVI time series from 1986 to 2025. For the period of 1986–1999, annual NDVI was estimated based on surface reflectance datasets from Landsat 5 and Landsat 7 (30 m spatial resolution, 16-day revisit time). The NDVI formula is expressed as follows [27]:

$$\mathrm{NDVI} = \frac{\rho_{NIR} - \rho_{RED}}{\rho_{NIR} + \rho_{RED}} \quad (1)$$

where ρ_{NIR} and ρ_{RED} represent the surface reflectance in the near-infrared and red bands, respectively.

From 2000 to 2025, MODIS MOD13Q1 data (250 m spatial resolution, 16-day composite) were used [28], with the NDVI band calibrated as follows:

$$\mathrm{NDVI} = DN \times 0.0001 \quad (2)$$

The SummaryQA quality band (retaining levels 0 and 1) was employed to mask out invalid pixels, such as clouds and snow/ice. For each year, the arithmetic mean of all valid observations was calculated to obtain the annual mean NDVI. Finally, the data were uniformly clipped to the vector boundary of the study area watershed, outputting one GeoTIFF per year.

The two products were used directly for their respective periods (Landsat 1986–1999; MODIS 2000–2025) without radiometric cross-calibration. Neither decline reported in Section 4.2 spans this point (1991–1995 falls in Landsat, 2006–2010 in MODIS), and all between-class comparisons are made within single years. NDVI change rates were quantified using the Sen slope estimator for each pixel (NDVI decade^{-1}), with the Mann–Kendall test used to assess significance. Trends were estimated from the 40 annual values (1986–2025); five-year period means appear only in the display maps of Figures 3 and 4.

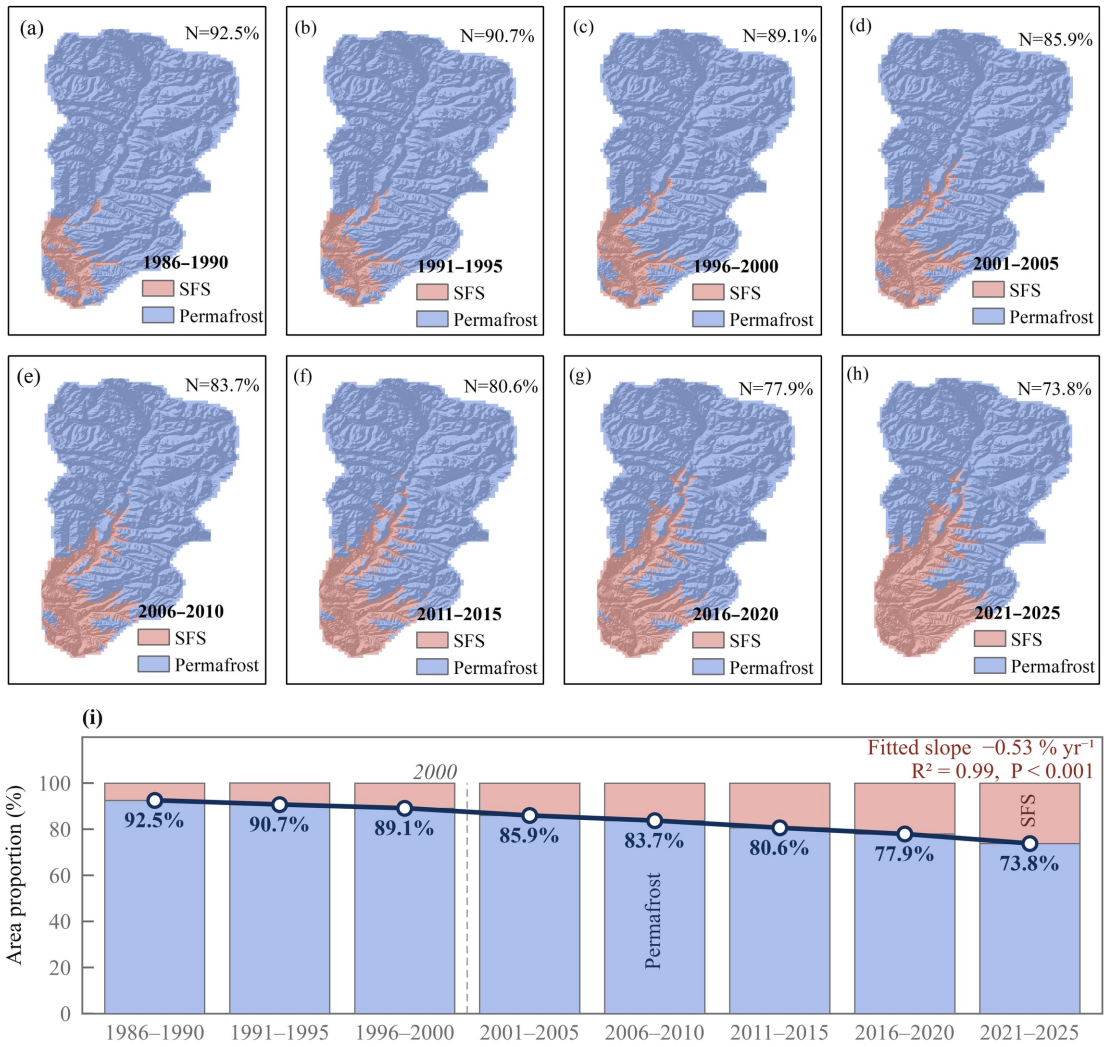

Figure 3. Changes in permafrost area in the study area. (**a**) 1986–1990; (**b**) 1991–1995; (**c**) 1996–2000; (**d**) 2001–2005; (**e**) 2006–2010; (**f**) 2011–2015; (**g**) 2016–2020; (**h**) 2021–2025; (**i**) Area proportions of Permafrost and SFS in each period (stacked bars), with the permafrost proportion shown as a line; the fitted linear trend is given in the panel.

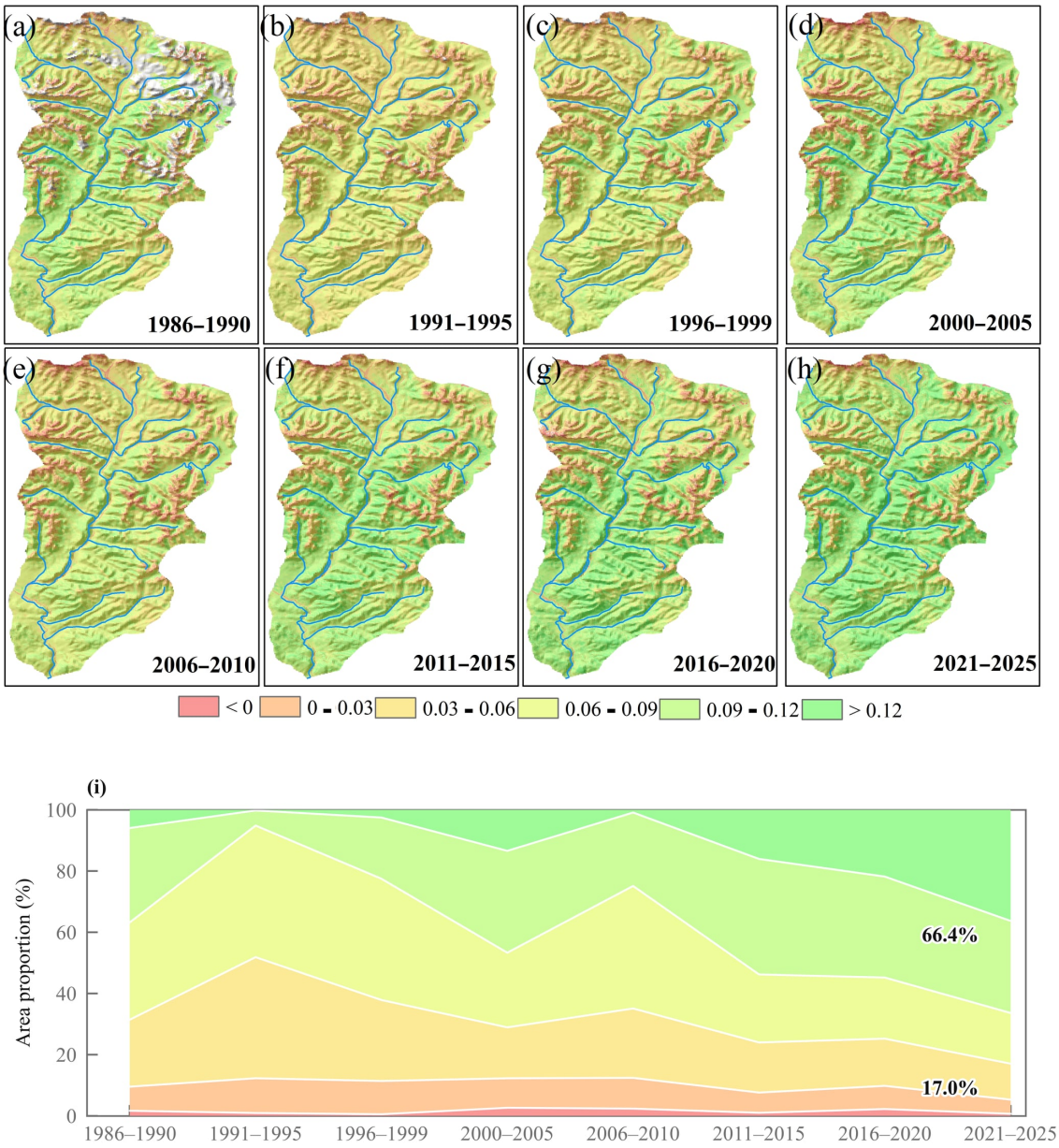

Figure 4. Spatiotemporal changes in NDVI across the study area. (**a**) 1986–1990; (**b**) 1991–1995; (**c**) 1996–1999; (**d**) 2000–2005; (**e**) 2006–2010; (**f**) 2011–2015; (**g**) 2016–2020; (**h**) 2021–2025; (**i**) Proportions of the six NDVI classes in each period (stacked area); values at the right denote the cumulative proportion of NDVI < 0.06 (17.0%) and NDVI ≥ 0.09 (66.4%) in 2021–2025. (Note: Panels (**c**,**d**) use the specified time intervals because the applied datasets are temporally segmented between 1999 and 2000.)

3.5. Mann–Kendall (MK) Trend Test

This study employed the Mann–Kendall (MK) non-parametric statistical test to assess the significance of the NDVI change rates across the study area [29,30]:

$$Z = \begin{cases} \frac{S-1}{\sqrt{Var(S)}} & (S > 0) \\ 0 & (S = 0) \\ \frac{S+1}{\sqrt{Var(S)}} & (S < 0) \end{cases} \quad (3)$$

where S is the cumulative sum of the sign function (sgn) of the differences between all dual observations in the time series, and $Var(S)$ is the variance of the statistic S. At a given significance level α, the trend is considered significant if the absolute value of the calculated

Z exceeds the critical value $Z_{(1-\alpha/2)}$ from the standard normal distribution. For instance, $|Z| \geq 1.96$ and $|Z| \geq 2.58$ indicate significance at the 0.05 and 0.01 levels, respectively.

3.6. Structural Equation Modeling

SEM was employed to quantitatively dissect the direct and indirect coupled mechanisms by which air temperature, precipitation, and permafrost thermal state affect NDVI dynamics. The matrix equation for the core structural model of SEM is expressed as follows [19]:

$$y = By + \Gamma x + \zeta \quad (4)$$

where y is the vector of endogenous variables (variables whose values are determined by other variables within the model, i.e., the rates of change in the F-index and NDVI in this study); x is the vector of exogenous driving variables (independent external drivers not influenced by the model, i.e., the rates of change in air temperature and precipitation); B and Γ are the standardized path coefficient matrices representing the relationships among endogenous variables and the effects of exogenous variables on endogenous variables, respectively; and ζ is the residual vector. Model parameters were estimated using the Maximum Likelihood (ML) method.

4. Results

4.1. Permafrost Changes

Between 1986 and 2025, the permafrost extent in the study area exhibited a continuous shrinking trend (Figure 3). The permafrost coverage peaked at 92.5% during the 1986–1990 period and subsequently declined in each consecutive stage, eventually dropping to 73.8% by 2021–2025. This represents a cumulative relative decrease of approximately 20.2% over the past four decades. Linear fitting results indicate that the permafrost area decreased at an overall rate of approximately 0.53% yr^{-1}, exhibiting a highly significant temporal trend ($R^2 \approx 0.99$, $p < 0.001$). Examining the magnitude of change, the degradation process was stage dependent. The retreat was relatively slow before 2000 but progressively intensified thereafter, with a pronounced reduction of 4.1 percentage points occurring between the 2016–2020 and 2021–2025 periods, highlighting a recent acceleration in permafrost degradation.

Spatially, permafrost was initially widely distributed across the study area, with seasonally frozen soil (SFS) limited to a small extent in the southern region. Over time, the extent of SFS gradually expanded from the south toward the central region, extending along certain zonal corridors, while the original permafrost area steadily shrank. By 2021–2025, extensive areas in the south had transitioned into SFS, and the permafrost distribution in the central region exhibited pronounced contraction and fragmentation, whereas the northern region maintained a relatively high permafrost coverage. Overall, from 1986 to 2025, permafrost in the study area exhibited significant continuous and directional degradation, characterized by a stage-dependent pattern with late-stage acceleration.

4.2. Vegetation NDVI Changes

From 1986 to 2025, the composition of NDVI classes in the study area exhibited evident stage-dependent fluctuations but overall demonstrated a long-term trend shifting from low-to-moderate values to high values (Figure 4). The area was initially dominated by moderate NDVI regions but experienced a stage-specific decline between 1991 and 1995, during which the proportion of low-value classes (NDVI < 0.09) expanded significantly. However, high-value classes began to recover gradually after 1996. Despite a brief fluctuation from 2006 to 2010, the vegetation index rose continuously thereafter. By 2021–2025, the shift

toward high-value intervals reached its peak, with areas characterized by NDVI ≥ 0.09 surging to 66.4% of the study area. Concurrently, the area with NDVI < 0.06 shrank to 17.0%, indicating an overall significant enhancement in vegetation greenness.

Spatial distribution results further revealed that NDVI changes across different periods exhibited strong spatial heterogeneity. During 1986–1990, the study area was dominated by moderate NDVI regions (0.06–0.12). Moderate-to-high value patches were primarily distributed in the central–southern parts and certain river valleys, whereas the high-elevation mountains and localized slopes in the north still exhibited lower NDVI values. In 1991–1995, the low-to-moderate value regions expanded significantly; the 0.03–0.09 class formed large, continuous distributions across the study area, with a marked reduction in high-value patches. During the period from 1996 to 2005, moderate-to-high NDVI regions progressively recovered and expanded toward surrounding slopes. In particular, the spatial continuity of high-value green patches was markedly enhanced during 2001–2005. Although localized NDVI declines occurred during 2006–2010, causing short-term fluctuations in the expansion of high-value regions, the spatial pattern exhibited a relatively stable trend of shifting toward high values after 2011. From 2011 to 2020, regions with NDVI > 0.09 continuously expanded in the central and southern parts as well as areas adjacent to river valleys, gradually evolving from isolated patches into a more continuous distribution pattern. By 2021–2025, the area with NDVI > 0.12 increased substantially, forming distinct contiguous distributions in the central–southern part of the study area, while low-value regions primarily persisted in the north and along certain ridges and steep slopes. Overall, despite distinct interdecadal fluctuations in NDVI across the study area from 1986 to 2025, the long-term changes were primarily characterized by the expansion of high-value regions, the contraction of low-to-moderate value regions, and enhanced spatial connectivity. This trend became even more prominent after 2011.

4.3. NDVI Change Rates and Trend Significance

The spatial pattern of NDVI change rates in the study area from 1986 to 2025 was predominantly characterized by positive increases alongside localized declines, indicating an overall significant trend of vegetation growth (Figure 5). The spatial distribution of NDVI change rates revealed that most areas exhibited values greater than 0. Specifically, zones with positive change rates of 0.010–0.025 and >0.025 were widely distributed, primarily concentrated in the central–southern river valleys, gentle slopes, and certain low-elevation areas, forming localized contiguous patches. This indicates a sustained increase in NDVI across these regions throughout the study period. In contrast, areas with negative NDVI change rates (<0) covered a relatively small area. These were predominantly distributed in strip or patch-like patterns across the northern and central-eastern regions, as well as along certain ridges and steep slopes, showing a clear spatial correspondence with areas of high topographic relief. Zones with slight increases (0–0.010) were mostly situated between the positive and negative change zones, exhibiting distinct transitional characteristics.

The Mann–Kendall (MK) trend significance test further demonstrated that the long-term NDVI dynamics in the study area possessed high statistical significance. Regions exhibiting highly significant changes ($p < 0.01$) dominated the study area, extensively covering the central and southern sectors, as well as most river valleys and hillslopes. Zones with significant changes ($0.01 \leq p < 0.05$) were primarily distributed as scattered patches or narrow bands across specific mountainous and high-elevation terrains. Conversely, non-significant regions ($p > 0.05$) were relatively limited in extent, mainly concentrated in the northern and northeastern parts and along certain ridges. These regions spatially overlapped to some degree with areas experiencing low or negative NDVI change rates. Synthesizing the change rates and MK test results reveals that the NDVI in the study area

over the past four decades experienced predominantly significant increases. Regions with high change rates generally exhibited high trend significance, whereas localized areas of vegetation decline or weak change were largely confined to mountainous zones with strong topographic relief. This underscores the pronounced spatial heterogeneity in long-term NDVI dynamics.

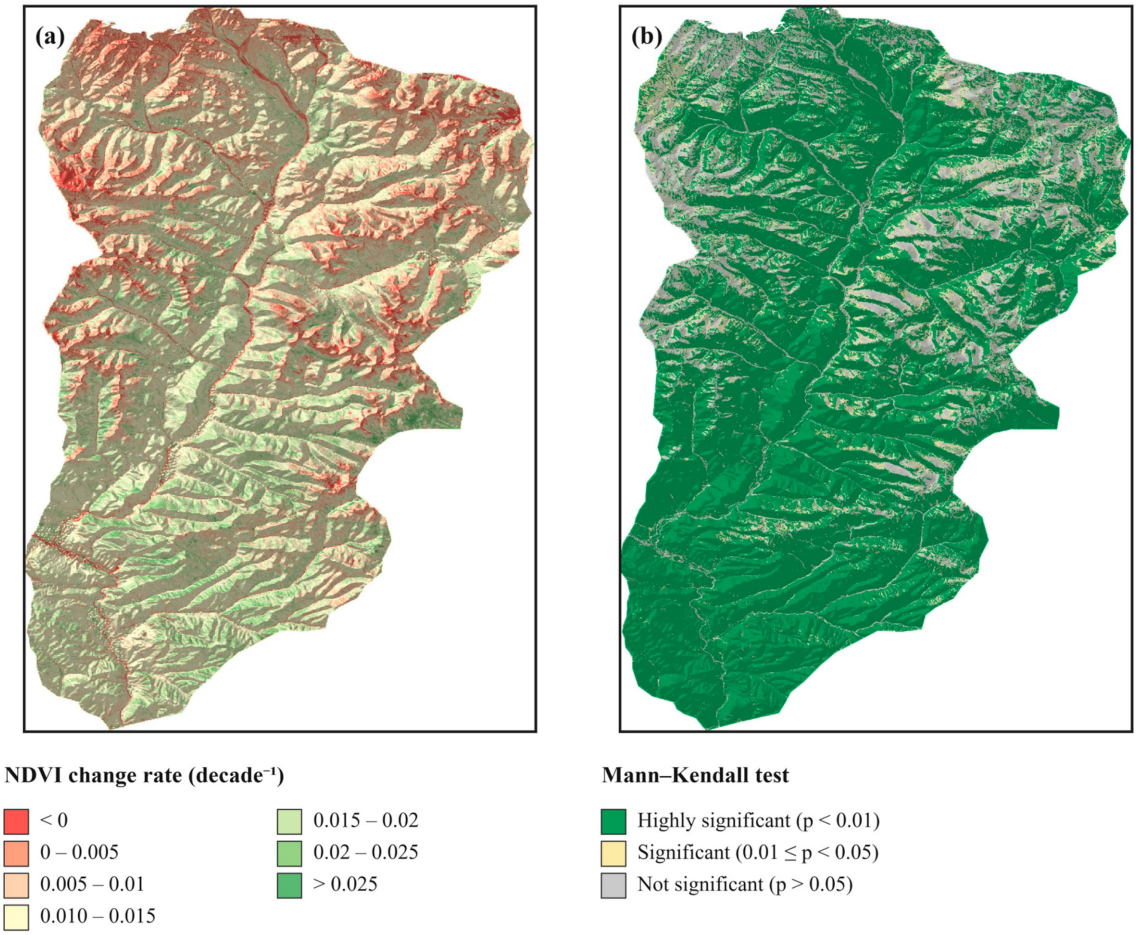

Figure 5. Changes in NDVI across the study area, 1986–2025. (**a**) Sen's slope of annual NDVI (NDVI decade^{-1}); (**b**) Mann–Kendall significance test. Panel (**b**) shows the significance level only; the direction and magnitude of change are given in (**a**).

4.4. Relationships Between NDVI Changes and Environmental Factors

To investigate the impact of permafrost state changes on vegetation dynamics, we further compared the NDVI characteristics among three distinct temporal trajectories from 1986 to 2025: areas where permafrost persisted throughout the entire study period (Persistent Permafrost), areas that remained as seasonally frozen soil throughout the period (Persistent SFS), and areas where permafrost completely thawed and converted into seasonally frozen soil during the period (Degraded Permafrost). These three classes describe the temporal persistence of the freeze state and are distinct from the geographical categories of continuous, discontinuous, sporadic and isolated permafrost, which are defined by areal extent. The results demonstrated distinct differences in NDVI and its change rates across different permafrost types (Figure 6). The mean NDVI from 1986 to 2025 exhibited a clear gradient across the three zone types. The Persistent Permafrost zone recorded the lowest mean NDVI, with a median of approximately 0.06, whereas the Persistent SFS and Degraded Permafrost zones saw their medians increase to approximately 0.07 and 0.08, respectively. The overall NDVI in the Degraded Permafrost zone was higher than in the other two zones, with a more

concentrated data distribution. This indicates that permafrost degradation, accompanied by improved surface thermal conditions and active layer deepening, provided a more favorable environment for vegetation growth. In contrast, vegetation productivity in the Persistent Permafrost zone was generally lower with a larger NDVI dispersion, constrained by prolonged low temperatures, a shallow active layer, and freeze–thaw processes, underscoring the pronounced limiting effect of the permafrost environment on vegetation development.

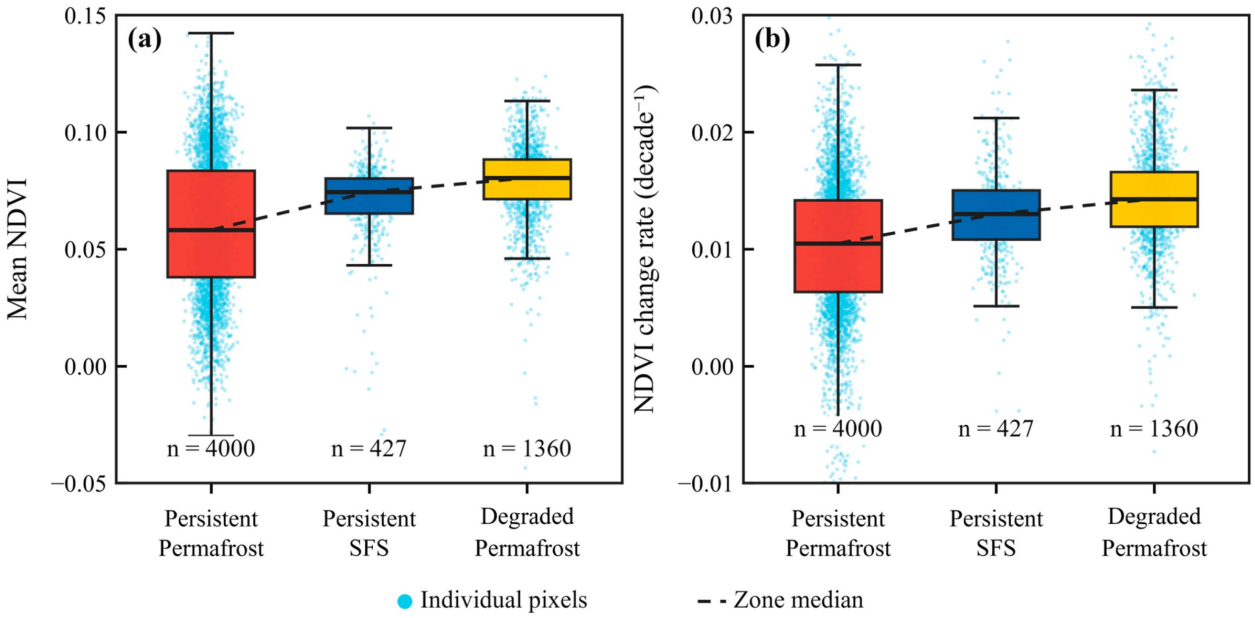

Figure 6. Permafrost degradation and NDVI changes. (**a**) Mean NDVI and (**b**) NDVI change rate in three zones defined by their temporal trajectory from 1986 to 2025: Persistent Permafrost, Persistent SFS, and Degraded Permafrost. Boxes show the interquartile range with the median as a horizontal line, whiskers extend to 1.5 × IQR, light blue dots are individual pixels sampled randomly in proportion to area, and the dashed line connects the zone medians.

Regarding NDVI change rates, all three permafrost zones exhibited positive trends, indicating an overall recovery and improvement of vegetation in the study area over the study period (Figure 6b). Among them, the Persistent Permafrost zone had the lowest NDVI change rate, with a median of approximately 0.010 decade^{-1}; the rate increased to approximately 0.013 decade^{-1} in the Persistent SFS zone and peaked at approximately 0.014 decade^{-1} in the Degraded Permafrost zone. Compared to the Persistent Permafrost zone, the NDVI growth rate in the Degraded Permafrost zone increased by approximately 40%. This suggests that the permafrost degradation process likely facilitated rapid vegetation recovery by enhancing soil heat input, prolonging the growing season, and improving root-zone hydrothermal conditions. Further comparison revealed that the Degraded Permafrost zone possessed not only a higher mean NDVI level but also the highest NDVI growth trend, demonstrating a stronger vegetation response capacity in permafrost degradation areas over the past four decades.

To further elucidate the response characteristics of vegetation changes to environmental gradients in the study area, we analyzed the relationships between mean NDVI, NDVI change rates, and elevation, ground temperature, and active layer thickness (ALT) from 1986 to 2025. The results showed that both NDVI and its change rate exhibited significant responses to different environmental factors ($p < 0.01$); however, the direction of change and response patterns varied considerably (Figure 7).

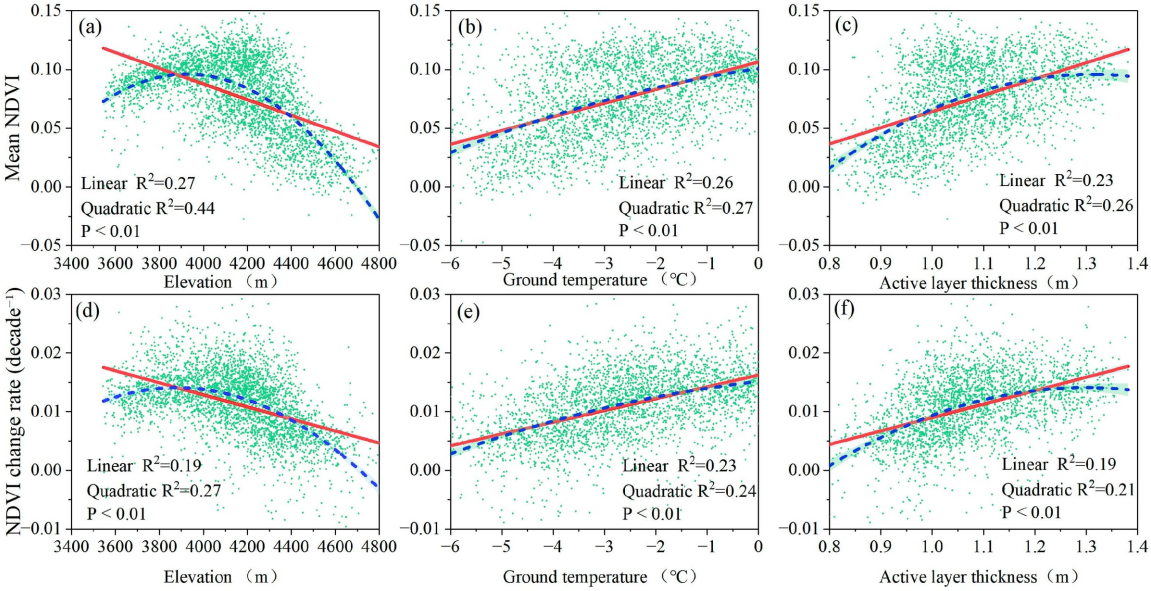

Figure 7. Relationships between environmental factors and NDVI. (**a**) Elevation and mean NDVI; (**b**) Ground temperature and mean NDVI; (**c**) ALT and mean NDVI; (**d**) Elevation and NDVI change rate; (**e**) Ground temperature and NDVI change rate; (**f**) ALT and NDVI change rate. Values in (**a**–**c**) are mean NDVI (dimensionless); values in (**d**–**f**) are Sen slopes of annual NDVI (NDVI decade^{-1}), estimated from the 40 annual values of 1986–2025; red and blue lines denote linear and quadratic fits, respectively. (Note: Panels (**a**,**d**) are based on the entire study area; panels (**b**,**c**,**e**,**f**) are based exclusively on the permafrost zone).

Along the elevational gradient, mean NDVI was significantly and negatively correlated with elevation (Figure 7a). The linear fitting ($R^2 = 0.27$) indicated an overall declining trend in vegetation coverage with increasing elevation. Nevertheless, the quadratic fitting yielded a higher explanatory power ($R^2 = 0.44$), suggesting a certain non-linear response of NDVI to elevational changes. NDVI reached a relatively high level within the 3800–4000 m range, and progressively decreased with further elevation increases, exhibiting a particularly sharp decline in areas above 4500 m. The NDVI change rate demonstrated a pattern similar to that of mean NDVI concerning elevation (Figure 7d). Both linear ($R^2 = 0.19$) and quadratic ($R^2 = 0.27$) fits indicated that the vegetation recovery rate was restricted at high elevations. As elevation increased, the rate of NDVI increase gradually diminished, even shifting to a negative growth trend at the highest elevations. This reflects the pronounced constraint of harsh alpine environmental conditions on the long-term evolution of vegetation.

By contrast, ground temperature exerted a significant promoting effect on NDVI. Mean NDVI showed an increasing trend with rising ground temperature (Figure 7b), with both linear ($R^2 = 0.26$) and quadratic ($R^2 = 0.27$) fittings yielding similar, relatively low explanatory power. This indicates that rather than a strict linear response, there is a weak monotonically increasing relationship between vegetation dynamics and improved thermal conditions. As ground temperatures rose from approximately −6 °C to 0 °C, the overall NDVI gradually increased from a lower baseline. The NDVI change rate was also significantly and positively correlated with ground temperature (Figure 7e). Both linear ($R^2 = 0.23$) and quadratic ($R^2 = 0.24$) fits suggested that higher temperature conditions facilitated the vegetation recovery process and elevated the NDVI growth rate. These results imply that in alpine ecosystems, thermal conditions are likely a critical environmental factor limiting vegetation growth and recovery.

A significant positive relationship was observed between ALT and NDVI. Mean NDVI increased continuously with thickening ALT (Figure 7c). The linear ($R^2 = 0.23$) and quadratic ($R^2 = 0.26$) fits suggested that a thicker active layer likely provides more favorable

hydrothermal and physical soil space conditions for vegetation root development. The quadratic fitting curve indicated that the increasing trend of NDVI leveled off when ALT exceeded approximately 1.2 m. The NDVI change rate also increased with deepening ALT (Figure 7f), with linear ($R^2 = 0.19$) and quadratic ($R^2 = 0.21$) fits implying that a deeper active layer favors long-term vegetation improvement. Overall, NDVI dynamics in the study area were co-regulated by topography, hydrothermal conditions, and the permafrost environment. Elevational increases exerted an inhibitory effect on vegetation, while rising ground temperatures and thickening active layers demonstrated pronounced promoting effects. These findings suggest that, as climate warming leads to improved thermal conditions and active layer deepening, vegetation in permafrost regions can obtain more advantageous growth conditions through enhanced soil hydrothermal exchanges during the growing season, thereby driving the continuous increase in NDVI over the past four decades.

5. Discussion

5.1. Permafrost Degradation and Its Spatial Heterogeneity

Between 1986 and 2025, the permafrost area in the study area steadily declined from 92.5% to 73.8%, experiencing a cumulative reduction of 18.7 percentage points. This corresponds to an overall degradation rate of approximately 0.53% yr^{-1}, underscoring a sustained degradation process over the past four decades. These results are broadly consistent with existing permafrost mapping across the Qinghai–Tibet Plateau (QTP), although the reference products differ in origin. The early compilation of Cheng et al., 1983–1996 [31] is a manual product, synthesizing survey records, aerial photographs and earlier thematic maps; the maps of Niu and Yin, 2003 [32], Zou et al., 2003–2012 [1] and Cao et al., 2010 [33] are model outputs obtained, respectively, from a decision-tree classifier applied to 1 km remote sensing data, the TTOP model driven by MODIS-derived freezing/thawing indices, and an extended frost-number model constrained by subregion survey maps; and the datasets of Ran et al., 2000–2015 [34] and Hu et al., 2010–2020 [35] are statistical and machine learning products, the former predicting MAGT from 1002 boreholes at 1 km and the latter a permafrost zonation index at 250 m from a rock glacier inventory using CatBoost. Despite these methodological differences, all indicate that the SFS extent expanded northward while the permafrost area continuously decreased. This tendency is not confined to the study area: both thermal-state monitoring and high-resolution mapping indicate progressive permafrost degradation across the QTP under continuous warming [34,35]. On a common relative basis, the 20.2% decline over four decades (0.51% yr^{-1}) is 1.2–1.4 times the plateau averages (0.37% yr^{-1} for 1980–2018 and ≈0.44% yr^{-1} for 2000–2020), consistent with the Qilian Mountains being a plateau hotspot but of the same order of magnitude [2,36]. This stage-dependent acceleration is also not unique to the study area: plateau-wide ALT thickening accelerated from 45 ± 15 to 86 ± 30 cm $10a^{-1}$ between 2001–2010 and 2011–2020 [37], although late-1990s cooling over the northwestern plateau indicates that its timing is not spatially uniform [2]; it is therefore best regarded as a plateau-wide tendency locally amplified by the marginal setting. This study further revealed the continuous degradation process in the study area over the past 40 years: the permafrost area decreased relatively slowly from 1986 to 2000, whereas the degradation rate accelerated significantly after 2000. Notably, the 2021–2025 period saw a reduction of 4.1 percentage points compared to 2016–2020, indicating a further intensification of the permafrost degradation process in recent years. This stage-dependent acceleration may be related to continuous regional warming, permafrost thermal inertia, and non-linear responses after approaching the thawing threshold. As permafrost ground temperatures gradually approach 0 °C, the thermal stability of the system diminishes; consequently, a relatively small heat input can trigger ground ice melting and

the conversion of permafrost types, thereby driving the transition from slow degradation to rapid retreat [26,38,39].

Spatially, the permafrost in the study area exhibited a distinct evolutionary pattern characterized by preferential degradation in the south, intensified fragmentation in the center, and relative stability in the north and high-elevation regions. Permafrost distribution maps across different decades consistently indicate that SFS was initially concentrated in the southern and low-elevation regions before progressively expanding toward the central region, while the permafrost extent steadily retreated toward the northern and high-elevation areas (Figure 8). This spatial shift aligns with the general permafrost distribution patterns on the QTP, reflecting the comprehensive regulatory effects of factors such as elevation, ground temperature, solar radiation, soil moisture, and land cover on permafrost thermal stability [39,40]. The southern and low-elevation regions typically possess higher ground temperatures and longer thawing periods; thus, their permafrost temperatures are closer to the critical thawing threshold, making them more sensitive to climate warming. Conversely, the northern and high-elevation regions, owing to lower ground temperatures and stronger cold reserves, still maintain higher stability. It is worth emphasizing that the permafrost distribution results for 2021–2025 in this study not only represent the latest permafrost state but were also thoroughly validated against borehole observations in 2025. The 15 m boreholes directly revealed that the active layer thickness at the drilling sites is approximately 2–3 m, beneath which thick layers of ice-rich soil and stratified ice exist at depths of 2.0 to 11.0 m in high-elevation sites (e.g., ZK6–ZK8). This deep stratigraphic evidence supports the reliability of the TPDC dataset applied in our local watershed. Therefore, they possess high spatial reliability and can accurately reflect the current permafrost landscape. Compared to early permafrost distribution products based on regional surveys and low-to-moderate resolution remote sensing data, the late-stage results of this study have further enhanced the capability of permafrost identification at the local scale. Consequently, the decline in permafrost area from 2021 to 2025 more likely reflects an actual permafrost degradation process rather than artifacts of mapping errors. Overall, over the past four decades, the permafrost in the study area has gradually transitioned from a continuous coverage state to a fragmented and marginally retreating state, manifesting the long-term degradation trajectory of the alpine permafrost system under continuous climate warming.

5.2. Long-Term NDVI Increase and Its Interdecadal Fluctuations

From 1986 to 2025, the NDVI in the study area generally shifted from low-to-moderate to moderate-to-high values. Particularly after 2011, high-NDVI regions expanded continuously, with the area of NDVI $\geq$ 0.09 reaching 66.4% during 2021–2025. This indicates an overall increase in vegetation greenness across the study area over the past four decades. This trend aligns with existing research reporting the overall greening of the Qinghai–Tibet Plateau since the 1980s [41]. The greening rate obtained here (0.011 decade^{-1}) is slightly lower than, but of the same order of magnitude as, the plateau-wide average of 0.013 decade^{-1} reported for 1982–2020, indicating that the study area follows the regional greening trend rather than exceeding it in magnitude. Plant growth in alpine ecosystems has long been constrained by low temperatures and short growing seasons. Climate warming can ameliorate vegetation growth conditions by advancing soil thaw, prolonging the growing season, and accelerating nutrient cycling [9,42]. Further regional analyses indicated that this greening trend was not confined to low-elevation and gentle-slope areas. Although regions with elevations >4700 m generally exhibited lower NDVI values, their mean and median values increased overall over time, reaching a relatively high level during 2021–2025. Areas with slopes >15° displayed a similar long-term upward trend (Figure 9a,b). This demonstrates that even in regions with poor thermal conditions or strong topographic constraints, vegetation

greenness has generally improved over the past two decades, albeit with distinct variations in growth magnitude across different stages.

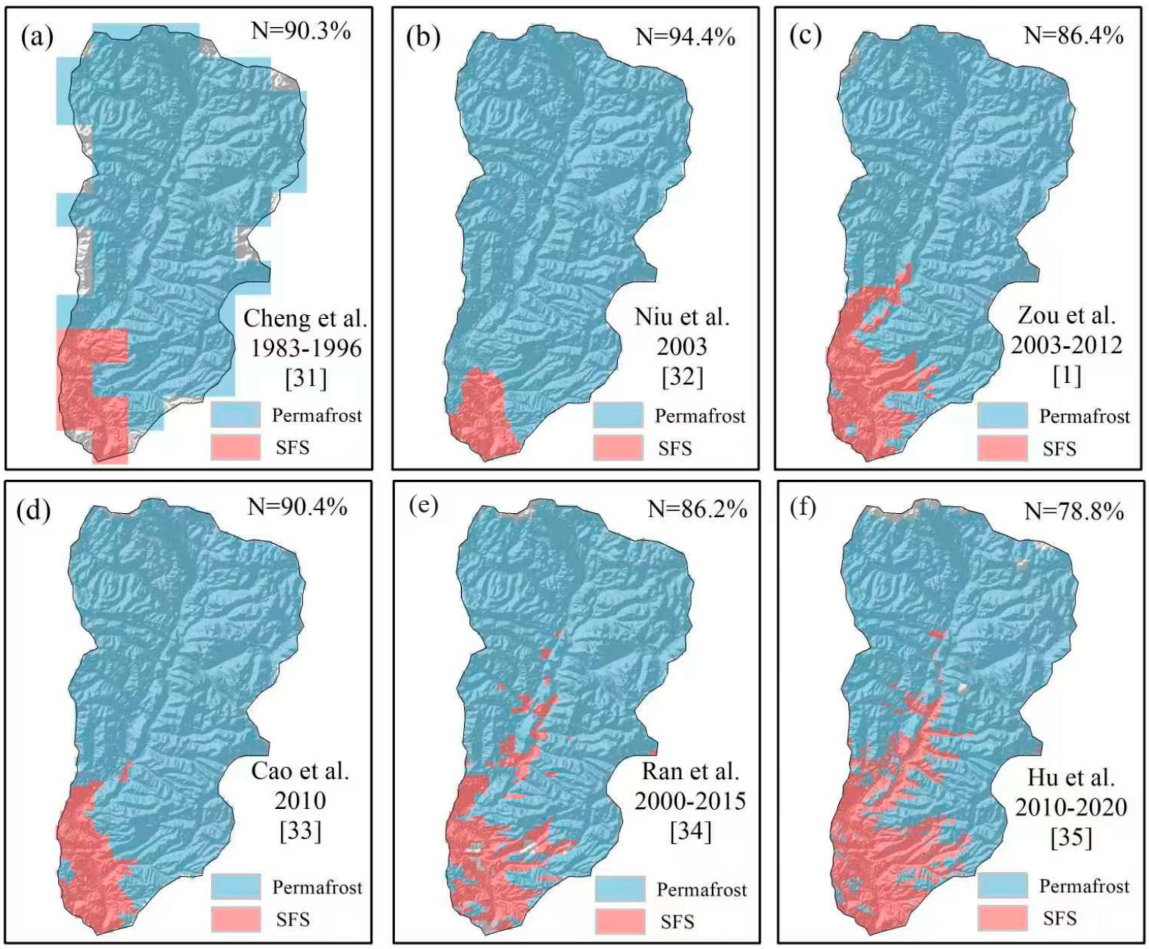

Figure 8. Reference permafrost maps of the study area across different time periods, redrawn from the sources indicated: (**a**) Cheng et al., 1983–1996 [31]; (**b**) Niu and Yin, 2003 [32]; (**c**) Zou et al., 2003–2012 [1]; (**d**) Cao et al., 2010 [33]; (**e**) Ran et al., 2000–2015 [34]; (**f**) Hu et al., 2010–2020 [35]. N denotes the proportion of permafrost area within the study area; years denote the epoch represented by each product and the bracketed numbers refer to the source publications.

NDVI changes exhibited significant interdecadal fluctuations and spatial heterogeneity. The entire study area experienced stage-dependent declines during 1991–1995 and 2006–2010. Correspondingly, the various topographic regions illustrated in Figure 9 also generally exhibited weakened growth or NDVI reduction around 2006–2010, followed by a subsequent rebound after 2011. This indicates that vegetation dynamics are not solely controlled by continuous warming but are the result of the combined effects of temperature, moisture, and topographic conditions. To test whether the NDVI–climate relationship is monotonic over the full record, we compared five-year means of NDVI with precipitation and temperature anomalies (Supplementary Figure S1). Across the eight periods, NDVI correlates more closely with precipitation ($r = 0.83$, $p = 0.011$) than with temperature ($r = 0.67$, $p = 0.067$), and the correlation with precipitation strengthens to $r = 0.93$ ($p = 0.003$) when 2006–2010—the only period with above-average precipitation but declining NDVI—is excluded. The non-monotonic behavior therefore reflects a shift between dry and wet phases rather than a change in the dominant climatic control. After controlling for longitude and elevation, both the NDVI and its change rate on the northern slopes were generally higher than those on the southern slopes (Figure 9c), demonstrating that aspect influences vegeta-

tion growth by regulating solar radiation, evapotranspiration, and soil moisture conditions. Similarly, the NDVI and its growth magnitude in the 37.5–37.6°N region were overall higher than those in the 38.0–38.1°N region (Figure 9d), revealing that regional thermal conditions, as represented by latitude, also exert a crucial modulatory effect. These results suggest that the long-term greening in the study area is highly ubiquitous; however, its intensity is significantly modulated by local hydrothermal conditions shaped by elevation, slope, aspect, and latitude. This aligns with existing understandings that vegetation dynamics on the QTP are characterized by pronounced topographic dependence and moisture constraints [9,43]. Therefore, it is more appropriate to interpret the long-term increase in NDVI observed in this study as a vegetation greenness response co-regulated by permafrost, moisture, and topographic conditions under a regional warming background, rather than simply equating it to a synchronous enhancement of ecosystem productivity or ecological quality. Additionally, because strict cross-calibration was not performed between the Landsat and MODIS datasets, the observed interdecadal NDVI fluctuations might contain inherent uncertainties introduced by sensor differences, which should be carefully considered in future fine-scale assessments.

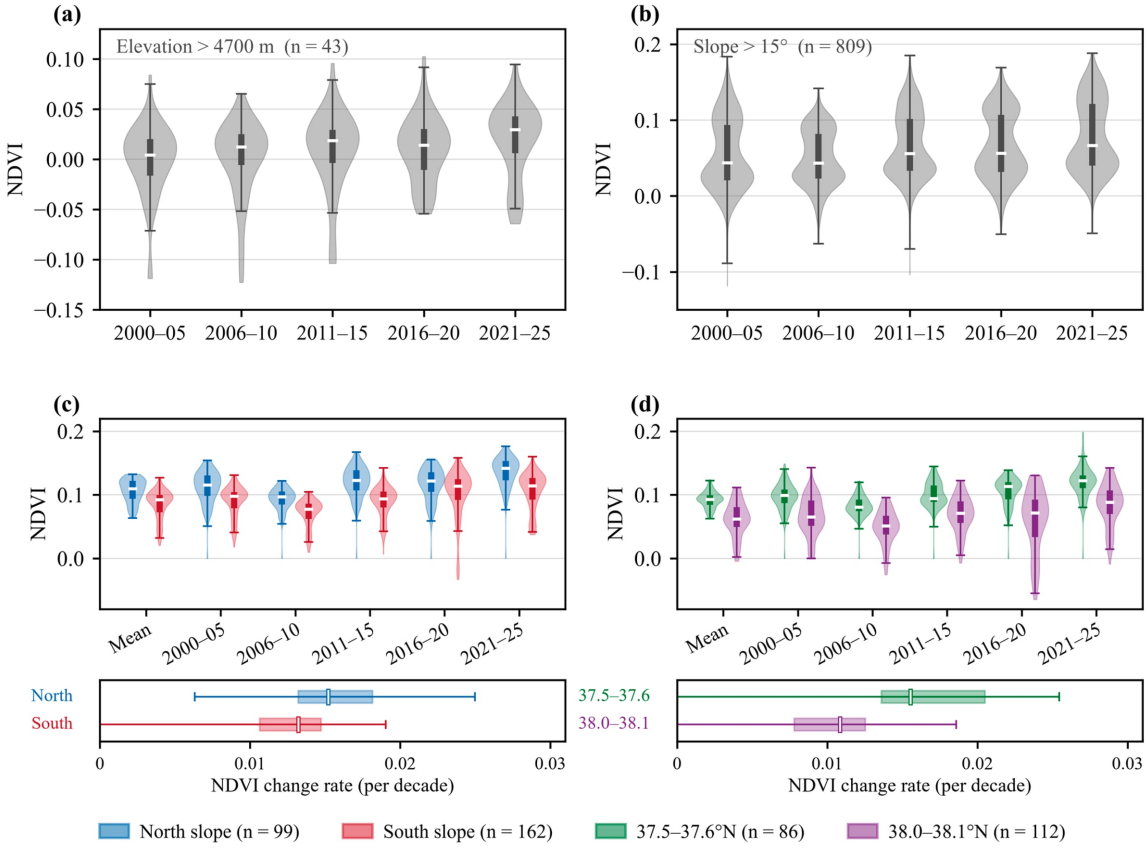

Figure 9. NDVI and its change rate in different regions. Distributions are shown as violins (kernel density), with the thick vertical bar marking the interquartile range, the white tick the median, and the thin line the 1.5 × IQR whiskers. (**a**) NDVI by period above 4700 m (n = 43). (**b**) NDVI by period where slope >15° (n = 809). (**c**) NDVI by period on north-facing (blue, n = 99) and south-facing (red, n = 162) slopes at similar longitudes and elevations (3950–4050 m); the lower strip gives the corresponding NDVI change rates on a separate axis. (**d**) NDVI by period in two latitude bands at similar longitudes and elevations (37.5–37.6°N, green, n = 86; 38.0–38.1°N, purple, n = 112); the lower strip gives the corresponding NDVI change rates. "Mean" denotes the period mean of each point. All subsets were drawn from a single set of 5000 points sampled randomly and uniformly from the valid pixels of the study area, so the size of each subset reflects the proportion of the study area occupied by the corresponding terrain class rather than a fixed sampling design.

5.3. Co-Regulation of NDVI Changes by Permafrost State, Air Temperature, and Precipitation

A clear NDVI gradient existed among different permafrost types: the Persistent Permafrost zone exhibited the lowest mean NDVI and change rate, the Persistent SFS zone was intermediate, and the Degraded Permafrost zone showed the highest values. Notably, the NDVI change rate in the Degraded Permafrost zone was approximately 0.014 decade^{-1}, representing an increase of about 40% compared to the Persistent Permafrost zone. This result indicates a distinct positive correlation between permafrost degradation and increased vegetation greenness within the spatiotemporal scope of this study. The underlying mechanism is likely that the initial stage of permafrost degradation is typically accompanied by rising ground temperatures and active layer thickening. These changes can expand the physical soil space available for plant roots, prolong the frost-free period, and enhance the availability of liquid water and nutrients, thereby temporarily alleviating the thermal limitations on alpine plants [15,44]. However, this relationship is not unidirectionally facilitative. Previous studies have demonstrated that excessive thickening of the active layer can intensify deep drainage and deplete soil moisture in the root zone, subsequently leading to declines in biomass and species richness [6]. Therefore, it is more appropriate to interpret our findings as follows: at the current stage of degradation, the positive effects of improved thermal conditions and active layer deepening likely still outweigh the negative effects of root-zone moisture loss; however, as permafrost continues to degrade, this promoting effect may weaken or even reverse.

Analyses of elevation, ground temperature, and ALT further demonstrated that vegetation in the study area was co-regulated by multiple factors. Mean NDVI and its change rate generally decreased with increasing elevation, exhibiting a certain non-linear relationship. An optimal hydrothermal combination was likely formed within the 3800–4000 m range, whereas limitations such as low temperatures, short growing seasons, and thin soil layers intensified significantly above 4500 m [45]. Conversely, both ground temperature and ALT showed significant positive correlations with NDVI and its change rate, indicating that improved thermal conditions and active layer deepening are favorable to vegetation growth at the current stage. Nevertheless, the R^2 values of the respective models ranged only from 0.19 to 0.44, implying that a single factor can only explain a portion of the spatial variance; other variables such as precipitation, soil moisture, aspect, solar radiation, and human activities still play crucial roles [43,46,47]. Furthermore, the Degraded Permafrost zone may be inherently characterized by lower elevations and higher ground temperatures. Consequently, the current results primarily establish a correlation rather than conclusively confirming an independent causal role of permafrost degradation.

SEM was employed to further examine the statistical associations among these factors (Figure 10), with all path coefficients standardized. The temperature change rate showed a weak positive association with the NDVI change rate ($\beta = 0.28$, $p < 0.001$), whereas the direct association with precipitation was negligible ($\beta = -0.01$, $p = 0.66$). The F-index change rate was strongly and negatively associated with the NDVI change rate ($\beta = -0.56$, $p < 0.001$) and was itself more closely associated with precipitation ($\beta = 0.78$) than with temperature ($\beta = 0.09$). Because the F-index is derived from air temperature, its link to temperature is partly built into the definition, and the coefficient linking precipitation to the F-index most likely reflects the spatial co-variation in the two climate trends along the elevational gradient rather than an independent precipitation effect. In the Qilian Mountains, precipitation increases systematically with elevation across orogen-perpendicular transects [48], and the spatial pattern of the seasonal freeze state is likewise controlled primarily by altitude rather than latitude [49]. The two therefore co-vary along the same gradient without implying a direct causal link. The model therefore identifies the freeze-state index as the variable most closely tracking vegetation change, without establishing a verified physical pathway.

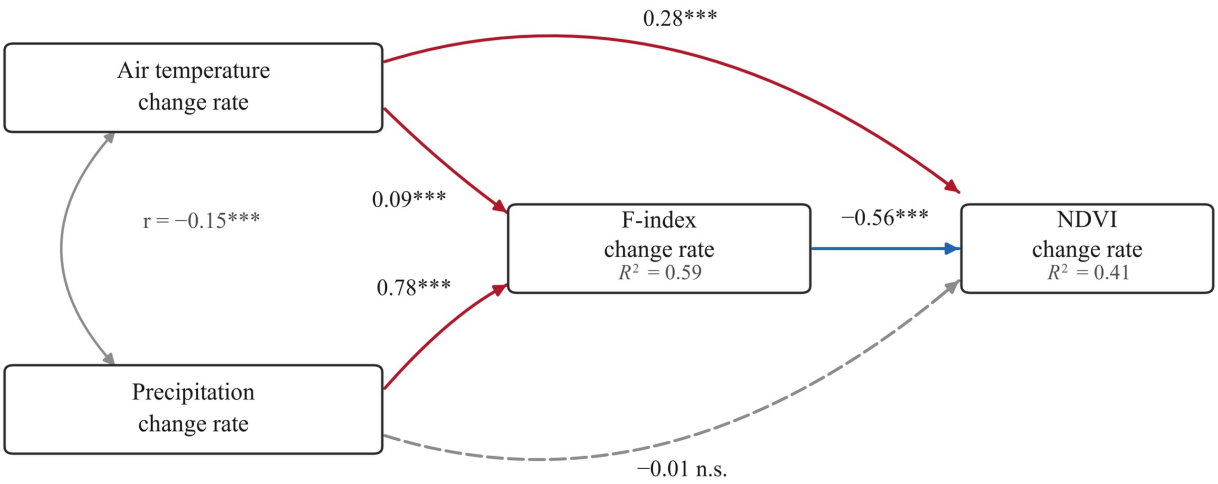

Figure 10. Structural equation model (SEM) of the statistical associations among the air temperature change rate, the precipitation change rate, the F-index change rate and the NDVI change rate. Values are standardized path coefficients. Red arrows denote positive associations, blue arrows negative ones, and the solid gray double-headed arrow the correlation between the two climate variables; the dashed gray arrow denotes a non-significant path ($p > 0.05$). R^2 is the variance explained for each endogenous variable. ***, $p < 0.001$; n.s., not significant.

5.4. Spatial Heterogeneity of NDVI Change Rates and Its Ecological Implications

The NDVI change rate results indicate that positive changes dominated the study area from 1986 to 2025. Regions with relatively high growth rates of 0.010–0.025 decade^{-1} and >0.025 decade^{-1} were widely distributed, presenting a pronounced overall vegetation greening trend. This is consistent with the prevalent vegetation greening pattern across the QTP [50]. The higher growth rates were primarily concentrated in the central–southern river valleys, gentle slopes, and certain low-elevation areas. In contrast, zones with negative or weak changes were mostly distributed in the northern regions, along high-elevation ridges, and in areas with complex terrains. The underlying reason may be that low- to mid-elevation regions benefit from improved thermal conditions coupled with favorable soil and moisture conditions, whereas high-elevation regions remain constrained by low temperatures, short growing seasons, thin soil layers. Previous studies have also demonstrated that the vegetation greening rate on the QTP generally decreases with rising elevation, indicating that warming cannot entirely offset the environmental constraints at high elevations [43].

An increase in NDVI primarily reflects enhanced vegetation greenness, which does not necessarily denote ecosystem recovery. As a limitation of this study, the lumped NDVI analysis might mask the specific successional dynamics of different communities, such as alpine meadows and alpine steppes, which may respond differently to permafrost degradation. Localized NDVI declines cannot be simply equated with ecological degradation, because shifts in plant community composition, shrub expansion, or hygrophyte-to-xerophyte species turnover can all alter NDVI without perfectly corresponding to changes in ecological functions [51,52]. Overall, vegetation in the study area was dominated by significant greening over the past four decades, yet its magnitude of change was distinctly modulated by elevation, topography, and hydrothermal conditions (Figures 7, 9 and 10). Additionally, anthropogenic interventions, represented by large-scale ecological restoration programs and grazing exclusion policies implemented since the early 2000s, have also played a certain promoting role in this widespread greening. However, given the geographical setting of the study area, its elevation range, ground-ice reserves and moisture supply represent only one segment of the pronounced east–west climatic gradient of the range [43,50]. Extrapolating the quantified relationships to the entire Qilian Mountains therefore requires further

calibration and validation against evidence from catchments with contrasting aridity and permafrost development.

6. Conclusions

This study elucidated the evolutionary characteristics and coupled regulatory mechanisms between permafrost degradation and vegetation dynamics in a typical alpine catchment of the Qilian Mountains from 1986 to 2025. The primary conclusions are as follows:

(1) Permafrost exhibited a continuous and stage-wise accelerated degradation pattern. Over the past four decades, the permafrost area in the study area decreased from 92.5% to 73.8% at a rate of approximately 0.53% yr^{-1}. Recently, it has demonstrated a significantly accelerated retreat, characterized by spatial heterogeneity with preferential degradation in the south and intensified fragmentation in the center.

(2) Vegetation experienced an overall significant greening with strong spatial heterogeneity. The NDVI structure in the study area distinctly shifted toward high-value intervals, with the high-value zone (NDVI $\geq$ 0.09) accounting for 66.4% of the area during 2021–2025. Vegetation improvement was predominantly concentrated in the central–southern river valleys and gentle slopes, and the greening rate was partly modulated by local topography.

(3) The permafrost thermal regime exerted a pronounced gradient effect on vegetation dynamics. The Degraded Permafrost zone possessed the highest vegetation coverage and the fastest greening rate (approximately 0.014 $decade^{-1}$), which was about 40% higher than that of the Persistent Permafrost zone. Surface warming and active layer deepening generally promoted vegetation growth; however, this promoting effect on vegetation improvement leveled off once the active layer thickened beyond approximately 1.2 m.

(4) The freeze-state index showed the strongest statistical association with vegetation dynamics ($\beta = -0.56$, $p < 0.001$), while the direct precipitation effect was negligible ($\beta = -0.01$, n.s.). Because the two climate variables co-vary along the elevational gradient, the high precipitation coefficient for the freeze-state index reflects their shared spatial pattern rather than an independent effect. The current greening may nevertheless weaken as ground ice is depleted.

Supplementary Materials: The following supporting information can be downloaded at: https://www.mdpi.com/article/10.3390/rs18223934/s1, Figure S1. Five-year means of NDVI and climatic anomalies in the Qilian Mountains, 1986–2025: (a) mean NDVI, (b) precipitation anomaly and (c) mean air-temperature anomaly for each five-year period, and (d) five-year mean NDVI plotted against precipitation anomaly. Anomalies are departures from the 1986–2025 mean. In (d), the solid line is the ordinary least-squares regression and the shaded band its 95% confidence interval, fitted to the seven periods shown as filled circles; 2006–2010 (open circle) was excluded from the fit because it is the only interval in which NDVI declined while precipitation was above the long-term mean. r, Pearson correlation coefficient; p, two-sided significance level; n, number of five-year periods.

Author Contributions: Conceptualization, Z.L. and X.F.; methodology, X.F. and X.W. (Xuyang Wu); software, X.W. (Xuhui Wang), Q.G. and X.Z.; validation, X.L.; formal analysis, X.W. (Xuhui Wang); investigation, X.W. (Xuhui Wang) and Q.G.; resources, Z.L. and X.F.; data curation, X.W. (Xuhui Wang) and Q.G.; writing—original draft preparation, X.W. (Xuhui Wang) and X.F.; writing—review and editing, X.W. (Xuhui Wang), X.F., Z.L. and X.W. (Xuyang Wu); visualization, X.Z. and X.L.; supervision, Z.L., X.F. and X.W. (Xuyang Wu); project administration, X.F. and X.W. (Xuyang Wu); funding acquisition, X.F. and Z.L. All authors have read and agreed to the published version of the manuscript.

Funding: This research was funded by the Open Fund for Field Scientific Observation and Research Station of Subalpine Ecosystem in the Central Qilian Mountains (QLSKFJJ-2024-D0004), Gansu Province Science and Technology Major Special Projects (Grant No. 26ZDFA004, 25ZDFA013), the Strategic Priority Research Program of the Chinese Academy of Sciences (Grant No. XDB0950200), the China Postdoctoral Science Foundation (2024M753468), the Program of the State Key Laboratory of Cryospheric Science and Frozen Soil Engineering, CAS (No. CSFSE-ZZ-2401).

Institutional Review Board Statement: Not applicable.

Informed Consent Statement: Not applicable.

Data Availability Statement: The climate background statistics were derived from the NASA POWER (MERRA-2) reanalysis, openly available at https://power.larc.nasa.gov/. The 1 km monthly air temperature and precipitation datasets and the permafrost datasets were obtained from the National Tibetan Plateau/Third Pole Environment Data Center (TPDC, https://data.tpdc.ac.cn/). Landsat 5/7 surface reflectance and MODIS MOD13Q1 imagery were accessed through the Google Earth Engine platform (https://code.earthengine.google.com/). The 100 m digital elevation model was obtained from the National Geospatial Data Cloud (NGDC, https://www.gscloud.cn/). The borehole drilling, stratigraphic, and ground temperature monitoring data collected by the authors are not publicly available because they are part of ongoing research; requests to access these data should be directed to the corresponding author.

Conflicts of Interest: The authors declare no conflicts of interest.

References

1. Zou, D.; Zhao, L.; Sheng, Y.; Chen, J.; Hu, G.; Wu, T.; Wu, J.; Xie, C.; Wu, X.; Pang, Q.; et al. A new map of permafrost distribution on the Tibetan Plateau. *Cryosphere* **2017**, *11*, 2527–2542. [CrossRef]
2. Ji, H.; Wu, X.; Zhao, S.; Nan, Z. Constrained simulation of permafrost thermal changes from 1980 to 2018 on the Qinghai–Tibet Plateau. *Glob. Planet. Change* **2026**, *263*, 105542. [CrossRef]
3. Jin, X.Y.; Jin, H.J.; Iwahana, G.; Marchenko, S.S.; Luo, D.L.; Li, X.Y.; Liang, S.H. Impacts of climate-induced permafrost degradation on vegetation: A review. *Adv. Clim. Change Res.* **2021**, *12*, 29–47. [CrossRef]
4. Liu, W.; Gao, Z.; Ding, Z.; Lin, Z.; Ran, Y.; Wang, Y.; Shao, P. Accelerated thermokarst lake expansion associated with ground ice melt in permafrost regions of the northwest Tibetan Plateau. *Permafr. Periglac. Process.* **2026**, e70063. [CrossRef]
5. Yang, M.; Nelson, F.E.; Shiklomanov, N.I.; Guo, D.; Wan, G. Permafrost degradation and its environmental effects on the Tibetan Plateau: A review of recent research. *Earth-Sci. Rev.* **2010**, *103*, 31–44. [CrossRef]
6. Jin, X.; Jin, H.; Luo, D.; Sheng, Y.; Wu, Q.; Wu, J.; Wang, W.; Huang, S.; Li, X.; Liang, S.; et al. Impacts of permafrost degradation on hydrology and vegetation in the source area of the Yellow River on northeastern Qinghai–Tibet Plateau, Southwest China. *Front. Earth Sci.* **2022**, *10*, 845824. [CrossRef]
7. Yi, S.; Zhou, Z.; Ren, S.; Xu, M.; Qin, Y.; Chen, S.; Ye, B. Effects of permafrost degradation on alpine grassland in a semi-arid basin on the Qinghai–Tibetan Plateau. *Environ. Res. Lett.* **2011**, *6*, 045403. [CrossRef]
8. Yang, Z.; Gao, J.; Zhao, L.; Xu, X.; Ouyang, H. Linking thaw depth with soil moisture and plant community composition: Effects of permafrost degradation on alpine ecosystems on the Qinghai–Tibet Plateau. *Plant Soil* **2013**, *367*, 687–700. [CrossRef]
9. Wang, X.; Yi, S.; Wu, Q.; Yang, K.; Ding, Y. The role of permafrost and soil water in distribution of alpine grassland and its NDVI dynamics on the Qinghai–Tibetan Plateau. *Glob. Planet. Change* **2016**, *147*, 40–53. [CrossRef]
10. Yun, H.; Zhu, Q.; Tang, J.; Zhang, W.; Chen, D.; Ciais, P.; Wu, Q.; Elberling, B. Warming, permafrost thaw and increased nitrogen availability as drivers for plant composition and growth across the Tibetan Plateau. *Soil Biol. Biochem* **2023**, *182*, 109041. [CrossRef]
11. Heijmans, M.M.P.D.; Magnússon, R.Í.; Lara, M.J.; Frost, G.V.; Myers-Smith, I.H.; van Huissteden, J.; Jorgenson, M.T.; Fedorov, A.N.; Epstein, H.E.; Lawrence, D.M.; et al. Tundra vegetation change and impacts on permafrost. *Nat. Rev. Earth Environ.* **2022**, *3*, 68–84. [CrossRef]
12. Li, N.; Wang, L.; Chen, D. Vegetation greening amplifies shallow soil temperature warming on the Tibetan Plateau. *npj Clim. Atmos. Sci.* **2024**, *7*, 118. [CrossRef]
13. Schuuring, S.; Halvorsen, R.; Eidesen, P.B.; Niittynen, P.; Kemppinen, J.; Lang, S.I. High Arctic vegetation communities with a thick moss layer slow active layer thaw. *J. Geophys. Res. Biogeosci.* **2024**, *129*, e2023JG007880. [CrossRef]
14. Peng, X.; Zhang, T.; Frauenfeld, O.W.; Wang, S.; Qiao, L.; Du, R.; Mu, C. Northern Hemisphere greening in association with warming permafrost. *J. Geophys. Res. Biogeosci.* **2020**, *125*, e2019JG005086. [CrossRef]
15. Yang, Y.; Wang, X.; Wang, T. Permafrost degradation induces the abrupt changes of vegetation NDVI in the Northern Hemisphere. *Earth's Future* **2024**, *12*, e2023EF004309. [CrossRef]

16. Berner, L.T.; Massey, R.; Jantz, P.; Forbes, B.C.; Macias-Fauria, M.; Myers-Smith, I.; Kumpula, T.; Gauthier, G.; Andreu-Hayles, L.; Gaglioti, B.V.; et al. Summer warming explains widespread but not uniform greening in the Arctic tundra biome. *Nat. Commun.* **2020**, *11*, 4621. [CrossRef] [PubMed]
17. Myers-Smith, I.H.; Kerby, J.T.; Phoenix, G.K.; Bjerke, J.W.; Epstein, H.E.; Assmann, J.J.; John, C.; Andreu-Hayles, L.; Angers-Blondin, S.; Beck, P.S.A.; et al. Complexity revealed in the greening of the Arctic. *Nat. Clim. Change* **2020**, *10*, 106–117. [CrossRef]
18. Anderson, J.E.; Douglas, T.A.; Barbato, R.A.; Saari, S. Linking vegetation cover and seasonal thaw depths in interior Alaska permafrost terrains using remote sensing. *Remote Sens. Environ.* **2019**, *233*, 111363. [CrossRef]
19. Grace, J.B. *Structural Equation Modeling and Natural Systems*; Cambridge University Press: Cambridge, UK, 2006.
20. Ding, Y.X.; Peng, S.Z. Spatiotemporal trends and attribution of drought across China from 1901–2100. *Sustainability* **2020**, *12*, 477. [CrossRef]
21. Peng, S.Z.; Ding, Y.X.; Wen, Z.M.; Chen, Y.M.; Cao, Y.; Ren, J.Y. Spatiotemporal change and trend analysis of potential evapotranspiration over the Loess Plateau of China during 2011–2100. *Agric. For. Meteorol.* **2017**, *233*, 183–194. [CrossRef]
22. Peng, S.Z.; Gang, C.; Cao, Y.; Chen, Y. Assessment of climate change trends over the Loess Plateau in China from 1901 to 2100. *Int. J. Climatol.* **2017**, *38*, 2250–2264. [CrossRef]
23. Peng, S.Z.; Ding, Y.X.; Liu, W.Z.; Li, Z. 1 km monthly temperature and precipitation dataset for China from 1901 to 2017. *Earth Syst. Sci. Data* **2019**, *11*, 1931–1946. [CrossRef]
24. Ni, J.; Wu, T.; Zhu, X.; Hu, G.; Zou, D.; Wu, X.; Li, R.; Xie, C.; Qiao, Y.; Pang, Q.; et al. Simulation of the present and future projection of permafrost on the Qinghai–Tibet Plateau with statistical and machine learning models. *J. Geophys. Res. Atmos.* **2021**, *126*, e2020JD033402. [CrossRef]
25. Niu, F.J.; Zheng, H.; Li, A. The study of frost heave mechanism of high-speed railway foundation by field-monitored data and indoor verification experiment. *Acta Geotech.* **2020**, *15*, 581–593. [CrossRef]
26. Wang, X.H.; Fan, X.W.; Yu, H.; Wu, X.Y.; Li, W.J.; Li, N.C.; Zhang, P.; Yu, L.Q.; Zhou, X.C.; Gao, Z.Y.; et al. Temporal and spatial variations in freezing–thawing indices and their impact on permafrost in the Himalayan region, China, from 1960 to 2020. *Adv. Clim. Change Res.* **2026**, *18*, 202–214. [CrossRef]
27. Tucker, C.J. Red and photographic infrared linear combinations for monitoring vegetation. *Remote Sens. Environ.* **1979**, *8*, 127–150. [CrossRef]
28. Didan, K. *MOD13Q1 MODIS/Terra Vegetation Indices 16-Day L3 Global 250 m SIN Grid V006*; NASA EOSDIS Land Processes DAAC: Sioux Falls, SD, USA, 2015. [CrossRef]
29. Mann, H.B. Nonparametric tests against trend. *Econometrica* **1945**, *13*, 245–259. [CrossRef]
30. Kendall, M.G. *Rank Correlation Methods*, 4th ed.; Charles Griffin: London, UK, 1975.
31. Cheng, G.; Li, S.; Nan, Z.; Tong, B. *Map of Permafrost on the Qinghai–Tibet Plateau (1:3,000,000) (1983–1996)*; National Tibetan Plateau/Third Pole Environment Data Center: Beijing, China, 2011. [CrossRef]
32. Niu, F.; Yin, G. *Map of the Frozen Soil in the Tibetan Plateau (2003)*; National Tibetan Plateau/Third Pole Environment Data Center: Beijing, China, 2018. [CrossRef]
33. Cao, Z.; Nan, Z.; Hu, J.; Chen, Y.; Zhang, Y. A new 2010 permafrost distribution map over the Qinghai–Tibet Plateau based on subregion survey maps: A benchmark for regional permafrost modeling. *Earth Syst. Sci. Data* **2023**, *15*, 3905–3930. [CrossRef]
34. Ran, Y.; Li, X.; Cheng, G.; Che, J.; Aalto, J.; Karjalainen, O.; Hjort, J.; Luoto, M.; Jin, H.; Obu, J.; et al. *High-Resolution Datasets of Permafrost Thermal State and Hydrothermal Zonation in the Northern Hemisphere*; National Tibetan Plateau/Third Pole Environment Data Center: Beijing, China, 2021. [CrossRef]
35. Hu, Z.; Yan, D.; Feng, M.; Xu, J.; Liang, S.; Sheng, Y. Enhancing mountainous permafrost mapping by leveraging a rock glacier inventory in northeastern Tibetan Plateau. *Int. J. Digit. Earth* **2024**, *17*, 2304077. [CrossRef]
36. Wen, B.; Zhang, T.; Zhou, X.; Yi, G.; Li, J.; Bie, X.; Chen, Y. Variation characteristics of frozen ground degradation in the Qinghai–Tibet Plateau observed using time series data of MODIS from 2000 to 2020. *Theor. Appl. Climatol.* **2023**, *151*, 1673–1686. [CrossRef]
37. Fu, Z.; Wu, Q.; Chen, A.; Wang, L.; Jiang, G.; Gao, S.; Yun, H.; Chen, J. Non-temperature environmental drivers modulate warming-induced 21st-century permafrost degradation on the Tibetan Plateau. *Nat. Commun.* **2025**, *16*, 7556. [CrossRef] [PubMed]
38. Biskaborn, B.K.; Smith, S.L.; Noetzli, J.; Matthes, H.; Vieira, G.; Streletskiy, D.A.; Schoeneich, P.; Romanovsky, V.E.; Lewkowicz, A.G.; Abramov, A.; et al. Permafrost is warming at a global scale. *Nat. Commun.* **2019**, *10*, 264. [CrossRef] [PubMed]
39. Zhao, L.; Hu, G.; Liu, G.; Zou, D.; Wang, Y.; Xiao, Y.; Du, E.; Wang, C.; Xing, Z.; Sun, Z.; et al. Investigation, monitoring, and simulation of permafrost on the Qinghai–Tibet Plateau: A review. *Permafr. Periglac. Process.* **2024**, *35*, 412–422. [CrossRef]
40. Chen, X.G.; Yu, Z.B.; Lin, H.; Shen, T.Q.; Jiang, P. Hydrological responses to permafrost degradation on Tibetan Plateau under changing climate. *Water Sci. Eng.* **2024**, *17*, 209–216. [CrossRef]
41. Liu, Y.; Xie, Y.; Guo, Z.; Xi, G. Effects of climate variability and human activities on vegetation dynamics across the Qinghai–Tibet Plateau from 1982 to 2020. *Remote Sens.* **2023**, *15*, 4988. [CrossRef]

42. Shen, M.; Piao, S.; Dorji, T.; Liu, Q.; Cong, N.; Chen, X.; An, S.; Wang, S.; Wang, T.; Zhang, G. Plant phenological responses to climate change on the Tibetan Plateau: Research status and challenges. *Natl. Sci. Rev.* **2015**, *2*, 454–467. [CrossRef]
43. Teng, H.; Luo, Z.; Chang, J.; Shi, Z.; Chen, S.; Zhou, Y.; Ciais, P.; Tian, H. Climate change-induced greening on the Tibetan Plateau modulated by mountainous characteristics. *Environ. Res. Lett.* **2021**, *16*, 064064. [CrossRef]
44. Yi, S.; Wang, X.; Qin, Y.; Xiang, B.; Ding, Y. Responses of alpine grassland on Qinghai–Tibetan Plateau to climate warming and permafrost degradation: A modeling perspective. *Environ. Res. Lett.* **2014**, *9*, 074014. [CrossRef]
45. Piao, S.; Cui, M.; Chen, A.; Wang, X.; Ciais, P.; Liu, J.; Tang, Y. Altitude and temperature dependence of change in the spring vegetation green-up date from 1982 to 2006 in the Qinghai–Xizang Plateau. *Agric. For. Meteorol.* **2011**, *151*, 1599–1608. [CrossRef]
46. Chen, B.; Zhang, X.; Tao, J.; Wu, J.; Wang, J.; Shi, P.; Zhang, Y.; Yu, C. The impact of climate change and anthropogenic activities on alpine grassland over the Qinghai–Tibet Plateau. *Agric. For. Meteorol.* **2014**, *189–190*, 11–18. [CrossRef]
47. Zhong, L.; Ma, Y.; Xue, Y.; Piao, S. Climate change trends and impacts on vegetation greening over the Tibetan Plateau. *J. Geophys. Res. Atmos.* **2019**, *124*, 7540–7552. [CrossRef]
48. Geng, H.; Pan, B.; Huang, B.; Cao, B.; Gao, H. The spatial distribution of precipitation and topography in the Qilian Shan Mountains, northeastern Tibetan Plateau. *Geomorphology* **2017**, *297*, 43–54. [CrossRef]
49. Wang, X.; Chen, R.; Han, C.; Yang, Y.; Liu, J.; Liu, Z.; Song, Y. Response of frozen ground under climate change in the Qilian Mountains, China. *Quat. Int.* **2019**, *523*, 10–15. [CrossRef]
50. Pang, G.; Wang, X.; Yang, M. Using the NDVI to identify variations in, and responses of, vegetation to climate change on the Tibetan Plateau from 1982 to 2012. *Quat. Int.* **2017**, *444*, 87–96. [CrossRef]
51. Piao, S.; Yin, G.; Tan, J.; Cheng, L.; Huang, M.; Li, Y.; Liu, R.; Mao, J.; Myneni, R.B.; Peng, S.; et al. Detection and attribution of vegetation greening trend in China over the last 30 years. *Glob. Change Biol.* **2015**, *21*, 1601–1609. [CrossRef] [PubMed]
52. Zhang, Y.; Piao, S.; Sun, Y.; Rogers, B.M.; Li, X.; Lian, X.; Liu, Z.; Chen, A.; Peñuelas, J. Future reversal of warming-enhanced vegetation productivity in the Northern Hemisphere. *Nat. Clim. Change* **2022**, *12*, 581–586. [CrossRef]

Disclaimer/Publisher's Note: The statements, opinions and data contained in all publications are solely those of the individual author(s) and contributor(s) and not of MDPI and/or the editor(s). MDPI and/or the editor(s) disclaim responsibility for any injury to people or property resulting from any ideas, methods, instructions or products referred to in the content.